Controlling Interactions between Quantum Emitters Using Atom Arrays

Taylor L. Patti, Dominik S. Wild, Ephraim Shahmoon, Mikhail D. Lukin, and Susanne F. Yelin

Controlling interactions between quantum emitters using atom arrays

Taylor L. Patti,[1, *] Dominik S. Wild,[1] Ephraim Shahmoon,[1, 2] Mikhail D. Lukin,[1] and Susanne F. Yelin[1, 3]

[1]*Department of Physics, Harvard University, Cambridge, Massachusetts 02138, USA*
[2]*Department of Chemical & Biological Physics, Weizmann Institute of Science, Rehovot 761001, Israel*
[3]*Department of Physics, University of Connecticut, Storrs, Connecticut 06269, USA*

We investigate the potential for two-dimensional atom arrays to modify the radiation and interaction of individual quantum emitters. Specifically, we demonstrate that control over the emission linewidths, resonant frequency shifts, and local driving field enhancement in impurity atoms is possible due to strong dipole-dipole interactions within ordered, subwavelength atom array configurations. We demonstrate that these effects can be used to dramatically enhance coherent dipole-dipole interactions between distant impurity atoms within an atom array. Possible experimental realizations and potential applications are discussed.

High-fidelity, deterministic interactions between individual quantum emitters and photons, as well as photon-mediated interactions between emitters, are central to quantum science and engineering [1–6]. In free space, these interactions are limited by the emitter's scattering cross section, which is typically bounded by a small geometrical limit [7]. To circumvent these limits, optical cavities and waveguides can be utilized to enhance interaction probabilities between atomic emitters [8–12]. Recent research has shown that photonic crystals can also engineer such atom-photon interactions [13–16]. While substantial experimental progress towards these goals has been made [17–22], widespread applications remain limited by multiple obstacles. For instance, many of these techniques require exquisite control of emitter arrays near or at nano-structured surfaces, which is experimentally challenging.

Coherent control of quantum emitters with 2D arrays furnishes inherent advantages over solid state architectures or classical dipole arrays, such as dynamic reconfigurability [24], substantially larger coherent coupling strengths [25], and environments devoid of surface imperfections [26]. Additionally, these systems feature intrinsic quantum nonlinearities and fermion-like behavior of interacting photons [27, 28]. While 1D atomic chains have been studied for coupling impurity atoms of broad and delocalized linewidth [29], and similar investigations have focused on other quantum emitters, such as superconducting qubits [30–32], only recently has it been shown that 2D optical atomic lattices, in contrast to their 1D counterparts, can interact strongly with individual photons [33–35]. In particular, the rich, two-dimensional mode structure of 2D arrays can provide a highly coherent interface capable of directional photon transfer [38] and a variety of other quantum information applications unfeasible in 1D geometries [27, 33, 36, 37, 39, 40].

In this Letter, we demonstrate that 2D atom arrays can be used to engineer emitter-photon interactions and to enable high-fidelity, long-range interactions between emitters. We consider impurity atom emitters
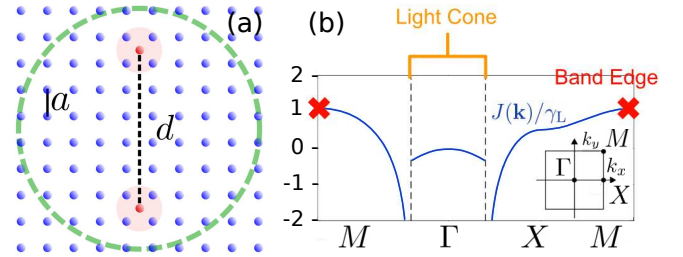

FIG. 1. (a) 2D array of atoms (blue) of interatomic spacing $a \lesssim \lambda$, for lattice atom transition wavelength λ, with impurity atoms (red) embedded xy-plane at plaquette centers and separated by distance d. While a free-space impurity has cross-section-limited light coupling (pink shading), its dipole-dipole interactions with the array extend over many lattice sites (dashed green circle). (b) Lattice normal mode frequency $J(\mathbf{k})$ vs momentum $\mathbf{k}$ of 2D atomic square lattice with spacing $a = 0.2\lambda$. The dispersion relation forms a photonic band structure, where Γ, X, and M are the symmetry points of a 2D square lattice Brillouin zone (inset).

(Fig. 1(a)). Atom arrays facilitate such interactions in a manner analogous to photonic materials or cavities, tailoring the environment of the impurity by selectively enhancing or suppressing the electromagnetic modes with which it interacts. The role of guided modes is taken by the arrays' normal modes, which form delocalized excitations of momentum $\mathbf{k}$, frequency $J(\mathbf{k})$, and decay rate $\Gamma(\mathbf{k})$. Each mode $\mathbf{k}$ couples to an impurity s in the array with dispersive and dissipative rates $\tilde{J}_s(\mathbf{k})$ and $\tilde{\Gamma}_s(\mathbf{k})$, respectively, effectively modifying its resonance frequency ω_I, linewidth γ_I, Rabi drive Ω_I, and dipole-dipole interactions with other impurity atoms. This allows one to confine and guide impurity emission within the 2D surface, and to engineer impurity-photon bound states that generate strong and coherent interaction between distant impurities. We extend the analogy between atom arrays and cavities by defining quality factors of impurity coupling to far-field light $Q^{(1)}$ and photon transfer between two impurities $Q^{(2)}$, which describe the number of co-
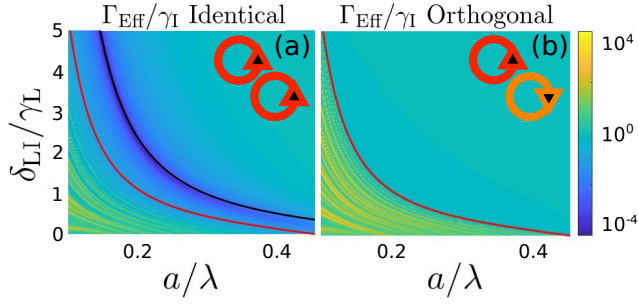
FIG. 2. Effective impurity linewidth Γ_{Eff} as a function of lattice spacing a and array atom detuning δ_{LI} for a 20×20 array. Both the identical (a) and orthogonal (b) configurations are shown (insets show relative circular polarizations of impurity and array). The band edge energy ω_{BE} is plotted in red. In (a), the black curve represents optimal lattice detuning $\delta_{\text{LI}}^{\text{D}}$ for suppressed impurity emission due to the lattice $\mathbf{k} = 0$ mode. Enhanced emission primarily occurs in (a) and (b) for $\delta_{\text{LI}} < \omega_{\text{BE}}$ due to resonant coupling between the impurity and lattice modes.

herent photon exchanges obtainable during the system's relaxation time [23].

We first summarize the formalism of an isolated array, in the absence of impurities [27, 33]. We consider a square 2D atom array in the xy-plane with lattice spacing $a \lesssim \lambda$, where $\omega_{\text{L}} = 2\pi c/\lambda$ is the resonance frequency of the lattice atoms (Fig. 1(a)). Subwavelength spacing is obtainable, e.g., using ultracold atoms in optical lattices [34, 41, 42]. Taking $\hbar = 1$ and lowering operators σ_i, the non-Hermitian Hamiltonian for the isolated N-atom array is

$$H = \sum_i^N \left(\omega_{\text{L}} - \frac{i}{2}\gamma_{\text{L}} \right) \sigma_i^\dagger \sigma_i + \sum_{i,j\neq i}^N \left(J_{ij} - \frac{i}{2}\Gamma_{ij} \right) \sigma_i^\dagger \sigma_j. \tag{1}$$

J_{ij} and Γ_{ij} are the coherent and dissipative parts of the free-space dipole-dipole interactions between the ith and jth lattice atoms separated by displacement vector $\mathbf{r}_{ij} = \mathbf{r}_i - \mathbf{r}_j$, where $J_{ij} - \frac{i}{2}\Gamma_{ij} = -\frac{3\pi\gamma_{\text{L}}}{\omega_{\text{L}}}\hat{d}_i^\dagger \cdot \mathbf{G}(\mathbf{r}_{ij}, \omega_{\text{L}}) \cdot \hat{d}_j$, for real-space Green's tensor $\mathbf{G}(\mathbf{r}, \omega)$ with normalized transition dipole vector $\hat{d}_i$ of atom i [43–46]. This formalism holds while the retardation of light within the spatial scale of our system is negligible [47]. In the limit of large lattices, Eq. (1) is diagonal in momentum space, yielding eigenstates that are collective surface modes of xy-plane quasimomentum $\mathbf{k}$, lowering operator $\sigma_{\mathbf{k}} = \frac{1}{\sqrt{N}}\sum_i^N e^{-i\mathbf{k}\cdot\mathbf{r}_i}\sigma_i$, and frequency shift and decay rate

$$J(\mathbf{k}) - \frac{i}{2}\Gamma(\mathbf{k}) = -\frac{3\pi\gamma_{\text{L}}}{\omega_{\text{L}}}\hat{d}_{\text{L}}^\dagger \cdot \mathbf{G}(\mathbf{k}, \omega_{\text{L}}) \cdot \hat{d}_{\text{L}} - \frac{i}{2}\gamma_{\text{L}}, \tag{2}$$

where $\mathbf{G}(\mathbf{k}, \omega_{\text{L}}) = \sum_{i,j\neq i}^N e^{-i\mathbf{k}\cdot\mathbf{r}_{ij}}\mathbf{G}(\mathbf{r}_{ij}, \omega_{\text{L}})$. This for-

malism represents frequencies $J(\mathbf{k})$ as a band structure of momentum modes (Fig. 1(b)), akin to those of photonic crystals. We indicate the highest energy level or band edge ω_{BE} as red crosses in Fig. 1(b) and red curves in Fig. 2(a) and (b). According to the wave equation, the momentum perpendicular to the array k_z of each $\mathbf{k}$ satisfies $\sqrt{\mathbf{k}^2 + k_z^2} = \omega_{\text{L}}$ for $c = 1$. For $a < \lambda/\sqrt{2}$, there exist guided modes $|\mathbf{k}| > \omega_{\text{L}}$ such that k_z is imaginary and the excitation is an evanescent mode, propagating along the lattice without loss [27, 33]. Conversely, modes for which $|\mathbf{k}| < \omega_{\text{L}}$ decay into the far-field and are said to be within the light cone (Fig. 1(b)).

We now introduce an impurity atom into the array interstitially [25]. Provided that $|\omega_{\text{I}} - \omega_{\text{L}}| \ll \omega_{\text{I}}, \omega_{\text{L}}$, the responses of both atomic species are narrow peaks around ω_{L} and the Green's tensor formalism holds [43–46]. This condition could also be fulfilled by a single atomic species by shifting one or more of the resonant frequencies using, e.g., an AC shift produced by optical tweezers. The coupling of an *impurity* with lowering operator s and position vector $\mathbf{r}_s$ to any surface excitation $\sigma_{\mathbf{k}}$ is described by the non-Hermitian Hamiltonian under the rotating wave approximation

$$H = -i\frac{\gamma_{\text{I}}}{2}s^\dagger s - \sum_{\mathbf{k}} \left[\delta_{\text{LI}} - J(\mathbf{k}) + i\frac{\Gamma(\mathbf{k})}{2} \right] \sigma_{\mathbf{k}}^\dagger \sigma_{\mathbf{k}}$$
$$+ \sum_{\mathbf{k}} \left[\tilde{J}_s(\mathbf{k}) - i\frac{\tilde{\Gamma}_s(\mathbf{k})}{2} \right] \sigma_{\mathbf{k}}^\dagger s + \sum_{\mathbf{k}} \left[\tilde{J}_s(\mathbf{k})^* - i\frac{\tilde{\Gamma}_s(\mathbf{k})^*}{2} \right] s^\dagger \sigma_{\mathbf{k}}, \tag{3}$$

where

$$\tilde{J}_s(\mathbf{k}) - \frac{i}{2}\tilde{\Gamma}_s(\mathbf{k}) = -\frac{3\pi\sqrt{\gamma_{\text{I}}\gamma_{\text{L}}}}{\omega_{\text{L}}}\hat{d}_{\text{L}}^\dagger \cdot \tilde{\mathbf{G}}_s(\mathbf{k}, \omega_{\text{L}}) \cdot \hat{d}_{\text{I}}, \tag{4}$$

$\tilde{\mathbf{G}}_s(\mathbf{k}, \omega_{\text{L}}) = \sum_i^N e^{-i\mathbf{k}\cdot\mathbf{r}_i}\mathbf{G}(\mathbf{r}_{is}, \omega_{\text{L}})$, and $\delta_{\text{LI}} = \omega_{\text{I}} - \omega_{\text{L}}$.

As seen from Eq. (4), the coupling between the impurity and lattice atoms depends on their relative polarization. We assume that all atoms have either right or left-handed circular polarization in the xy-plane and identify the two polarization configurations key to this work: (1) the identical configuration, where both the lattice and impurity atoms have the same polarization (e.g. both right-handed) and (2) the orthogonal configuration, where the lattice and impurity atoms have the opposite polarization (e.g. right and left-handed, see Fig. S2). These polarizations could be individually addressed by inducing Zeeman shifts with a z-axis magnetic field. The orthogonal configuration still leads to impurity-lattice interaction, as these polarizations are only orthogonal for light emitted along the z-axis, not within the xy-plane.

To gain intuition for the distinct effects of these two polarization configurations, we study a toy model: an impurity in a 2×2 atom array, with details derived in the

Supplementary Material (SM) [25]. The impurity only couples to two of four array modes: $\hat{v}_\parallel$, the lowest momentum mode with the largest linewidth, and $\hat{v}_\perp$, the highest momentum mode with the narrowest linewidth. In $\hat{v}_\parallel$, all atoms oscillate in-phase, whereas in $\hat{v}_\perp$ they oscillate π out-of-phase in a checkerboard pattern. These modes form the symmetry points of the Brillouin zone (Fig. 1(b)), with $\hat{v}_\parallel$ at the center (Γ) and $\hat{v}_\perp$ at the corner (M). An impurity in the orthogonal configuration only couples to $\hat{v}_\perp$ and an impurity in the identical configuration only couples to $\hat{v}_\parallel$. In this latter combination, the impurity and array oscillate π out-of-phase, forming a state comparable to a dark state in V-type electromagnetically induced transparency [48]. The orthogonal configuration impurity couples to $\hat{v}_\perp$, forming a bright state. The effect of the array on the impurity converges with relatively few atoms [25].

Provided that $\gamma_I \ll \gamma_L$, the array's dynamics occur on a time scale much shorter than that of the impurity s, rendering it a Markovian bath. To simultaneously fulfill this condition and the resonance frequency requirement, different isotopes of the same element could be used, e.g., ^{87}Sr and ^{88}Sr [29, 49]. Alternatively, tightly focused beams on select atoms could induce two-photon transitions by coupling them to metastable states, selectively tuning *both* the target atoms' resonance frequency and linewidth. The impurity exchanges photons, both real and virtual, with the array, giving rise to the so-called self-energy term Σ_{SE} through which the impurity is influenced by its own presence, reducing Eq. (3) to effective Hamiltonian $H_{Eff} = (\Sigma_{SE} - i\gamma_I/2) s^\dagger s$. Formally, the self-energy is computed from Eq. (3) by calculating the impurity's Schrodinger equation of motion and eliminating the array degrees of freedom by solving for the lattice modes in steady-state (Markovian bath) [25], yielding

$$\Sigma_{SE} = \sum_{\mathbf{k}} \frac{\left(\tilde{J}_s(\mathbf{k}) - \frac{i}{2}\tilde{\Gamma}_s(\mathbf{k})\right)\left(\tilde{J}_s^*(\mathbf{k}) - \frac{i}{2}\tilde{\Gamma}_s^*(\mathbf{k})\right)}{\delta_{LI} - J(\mathbf{k}) + \frac{i}{2}\Gamma(\mathbf{k})}. \quad (5)$$

The self-energy is key to understanding impurity-lattice interactions as it modifies the effective frequency and decay rate of the impurity to $\omega_{Eff} = \omega_I + \mathbf{Re}[\Sigma_{SE}]$ and $\Gamma_{Eff} = \gamma_I - 2\mathbf{Im}[\Sigma_{SE}]$, respectively. These equations are valid as long as Σ_{SE} varies little on the interval $\delta_{LI} + \mathbf{Re}[\Sigma_{SE}] \pm \Gamma_{Eff}$, such that the electromagnetic response of the lattice atoms with respect to δ_{LI} is approximately constant compared to that of the impurity atom. Under these same conditions, $\omega_{Eff} - \omega_L \approx \delta_{LI}$. For broad Γ_{Eff}, Σ_{SE} can vary considerably and non-Markovian analysis is valuable [15, 50].

Fig. 2(a) displays Γ_{Eff} in the identical configuration. Below ω_{BE} (red curve), Γ_{Eff} is enhanced as the impurity couples to resonant lattice modes, particularly those in the light cone. Above ω_{BE}, however, the linewidth of these states is suppressed by destructive interference be-
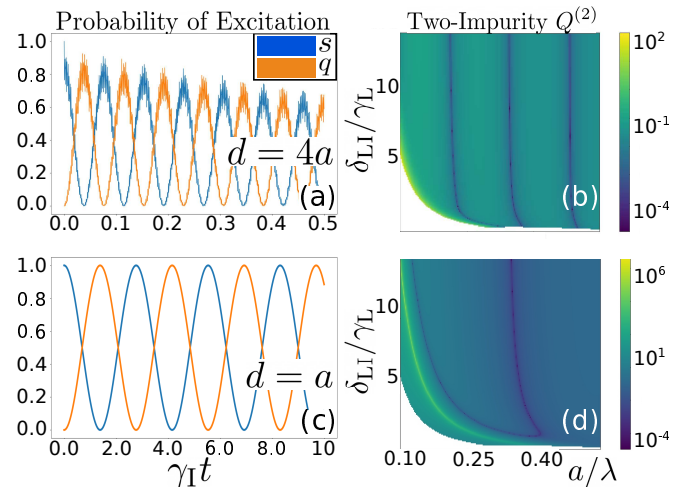

FIG. 3. Time-dependent transfer of excitation probability between initially excited s and initially ground state q in an array with $a = 0.1\lambda$ in (a) the orthogonal configuration at distance $d = 4a$ (for d dependence, see Fig. 4) and (c) the identical configuration at $d = a$. (b) Two-impurity quality factor $Q^{(2)}$ as a function of lattice spacing a and detuning δ_{LI} for the orthogonal configuration excitation transfer shown in (a), and (d) $Q^{(2)}$ of the identical configuration shown in (c). In (d), the yellow streak of high ($\sim 10^6$) $Q^{(2)}$ represents the minimal effective impurity linewidth Γ_{Eff} predicted by Eq. (6) with $\mathbf{k} = 0$. Likewise, in (b), $Q^{(2)}$ is maximized ($\sim 10^2$) for lattice detuning δ_{LI} near the band edge.

tween impurity radiation and off-resonant coupling with these modes. We can maximize the impurity lifetime (creating the "dark" state explained above) due to a particular $\sigma_{\mathbf{k}}$ by minimizing the corresponding term in Γ_{Eff} (maximizing Eq. (5)) with respect to δ_{LI}. As we place s at a plaquette center, $\tilde{J}_s(\mathbf{k})$, $\tilde{\Gamma}_s(\mathbf{k})$ are real, and we obtain the optimized lattice detuning

$$\delta_{LI}^D(\mathbf{k}) = J(\mathbf{k}) - \frac{\tilde{J}_s(\mathbf{k})\Gamma(\mathbf{k})}{\tilde{\Gamma}_s(\mathbf{k})}. \quad (6)$$

This quantity is plotted in black in Fig. 2(a) for $\mathbf{k} = 0$ and corresponds to the curve of smallest Γ_{Eff} and largest excitation probability. The correspondence of $\mathbf{k} = 0$ demonstrates that light cone coupling dominates identical configuration dynamics. In the SM, we show that linewidth suppression is lattice spacing limited, as $\Gamma_{Eff} \to 0$ in the limit $a/\lambda \ll 1$, while $\delta_{LI}^D \propto 1/a^3$ [25].

Fig. 2(b) depicts Γ_{Eff} in the orthogonal configuration. Like in the identical configuration, Γ_{Eff} is enhanced by impurity coupling to resonantly driven lattice modes for $\delta_{LI} < \omega_{BE}$. However, orthogonal configuration Γ_{Eff} has greater enhancement that occurs near resonance with the band edge, not the light cone.

If we add an incident driving field $\Omega_I s + \Omega_L(\mathbf{k})\sigma_{\mathbf{k}} + $ c.c. to Eq. (3), the impurity will experience both direct

Rabi drive Ω_I and an array-mediated driving response. Assuming that $\Omega_L(\mathbf{k})/\gamma_L \ll 1$, we eliminate the array degrees of freedom and find effective Rabi-frequency

$$\Omega_{\text{Eff}} = \sum_{\mathbf{k}} \frac{\left(\tilde{J}_s(\mathbf{k}) + \frac{i}{2}\tilde{\Gamma}_s(\mathbf{k})\right) \Omega_L(\mathbf{k})}{\delta_{\text{LI}} - J(\mathbf{k}) - \frac{i}{2}\Gamma(\mathbf{k})} + \Omega_I. \qquad (7)$$

The resultant single-impurity quality factor $Q^{(1)} = \Omega_{\text{Eff}}/\Gamma_{\text{Eff}}$ can be very large, indicating many coherent oscillations [23]. $\Omega_{\text{Eff}}/\Gamma_{\text{Eff}} \geq \Omega_I/\gamma_I$ for the identical polarization case with a weak, perpendicularly incident drive [25].

We now focus on lattice-mediated interactions between two impurities, s and q, which exchange photons via dipole-dipole interactions. This exchange has a lattice-independent component ϕ, which is simply the free-space dipole-dipole interaction between the impurities [51], and a lattice-mediated component, which represents the modification of the inter-impurity dipole-dipole interactions by lattice interactions. Eliminating the lattice degrees of freedom [25], the effective dipole-dipole interaction between s and q is $H_I^{(2)} = \Phi_{\text{Eff}}^{sq} s^\dagger q + \text{c.c.}$ [25] where

$$\Phi_{\text{Eff}}^{sq} = \sum_{\mathbf{k}} \frac{\left(\tilde{J}_s(\mathbf{k}) + \frac{i}{2}\tilde{\Gamma}_s(\mathbf{k})\right)\left(\tilde{J}_q(\mathbf{k})^* + \frac{i}{2}\tilde{\Gamma}_q(\mathbf{k})^*\right)}{\delta_{\text{LI}} - J(\mathbf{k}) - \frac{i}{2}\Gamma(\mathbf{k})} + \phi. \qquad (8)$$

The quantity Φ_{Eff}^{sq} is a key metric because it describes the lattice-mediated photon transfer between impurities, analogous to Eq. (7), but with the driving field replaced by that of the second impurity. Thus, Φ_{Eff}^{sq} depends on both the distance between impurities d and the placement of the impurities within their respective plaquettes. In regimes of large dissipative Φ_{Eff}^{sq}, the system experiences gain that can be interpreted as parity-time symmetry breaking [52].

When δ_{LI} is above the band edge (Markovian regime) and the impurities are identical, the photon transfer dynamics form an iSWAP gate between the impurities with interaction strength described by modified excitation transfer rate Φ_{Eff}^{sq} and decay rate Γ_{Eff}. As iSWAP gates have the necessary nonlinearity to be universal for quantum computation [53, 54], they serve as a basis for quantum computing architectures. This interaction results in coherent oscillations with large two-impurity quality factors (number of coherent excitation transfers [23]) $Q^{(2)} = \text{Re}[\Phi_{\text{Eff}}^{sq}]/\Gamma_{\text{Eff}}$ (Fig. 3). We now characterize $Q^{(2)}$ for both polarization configurations, highlighting the distinct advantages of each case.

Fig. 3(a) shows time-dependent transfer of excitation probability ($Q^{(2)} \sim 10^2$) between impurities s and q in the orthogonal configuration with $d = 0.4\lambda$ and $a = 0.1\lambda$. The high frequency, small amplitude modulations are induced by lattice mode interactions, especially those near
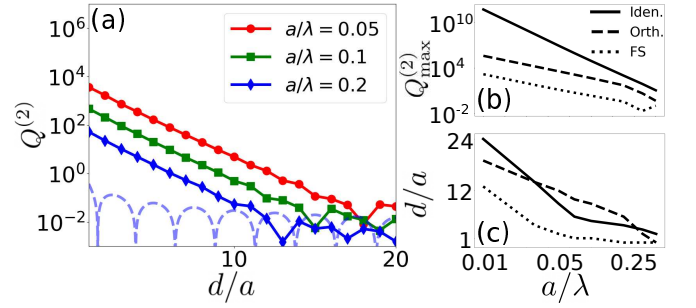

FIG. 4. (a) Number of coherent excitation transfers $Q^{(2)}$ between impurities s and q as a function of two-impurity separation d with various a in the orthogonal configuration. The value of $Q^{(2)}$ decreases exponentially with d due to the photon bound states that mediate this interaction [14, 15, 29]. Free-space $Q^{(2)}$ in units of $a/\lambda = 0.2$ (dashed light-blue) shown for comparison. (b) $Q_{\max}^{(2)} \equiv Q^{(2)}(d=a)$ as a function of a/λ for the identical (solid), orthogonal (dashed), and free space (dotted) configurations. (c) The largest number of lattice spacings d/a for which a $Q^{(2)} > 1$ scales roughly logarithmically with λ/a. All arrays are 40×40 with detunings $\delta_{\text{LI}} = 1.05\,\omega_{\text{BE}}$ (orthogonal) or $\delta_{\text{LI}} = \delta_{\text{LI}}^{\text{D}}(\mathbf{k}=0)$ (identical)

the band edge. As this coupling leads to impurity-lattice states outside of our Markovian approximation, the analytic value for orthogonal configuration $Q^{(2)}$ in Figs. 3(b) and 4 are slight overestimates [15], whereas the oscillations of Fig. 3(a) are exact numerical solutions. Fig. 3(b) is restricted to $\delta_{\text{LI}} > 1.05\,\omega_{\text{BE}}$ and $\delta_{\text{LI}} = 1.05\,\omega_{\text{BE}}$ in Fig. 3(a) to limit this error. The yellow regions show the strong coupling regimes near the band edge ($Q^{(2)} \sim 10^2$), while the dark blue lines represent regions of vanishing $Q^{(2)}$ occurring when the free-space and lattice mediated components of Φ_{Eff}^{sq} destructively interfere.

Strong impurity-impurity coupling also occurs in the identical configuration. Fig. 3(c) displays this highly-coherent ($Q^{(2)} \sim 10^5$) excitation probability transfer for $\delta_{\text{LI}} = \delta_{\text{LI}}^{\text{D}}(\mathbf{k} = 0)$ and $a = d = 0.1\lambda$. In general, identical configuration impurities reach large $Q^{(2)}$ values for $\delta_{\text{LI}} = \delta_{\text{LI}}^{\text{D}}(\mathbf{k} = 0)$ (Fig. 3(d)), where the two impurities in a Markovian bath approximation holds nearly exactly. This configuration also exhibits regions of low $Q^{(2)}$ due to vanishing Φ_{Eff}^{sq}.

For each polarization configuration, we examine the effect of impurity distance d and lattice spacing a on $Q^{(2)}$. Larger d weakens both free-space and array mediated dipole-dipole interactions, reducing Φ_{Eff}^{sq}. In the orthogonal configuration, $Q^{(2)}$ is proportional to $e^{-d/\xi}$ for some parameter dependent length scale ξ (Fig. 4(a)). This scaling is consistent with the width of exponentially localized impurity-array bound states [14, 15, 29] and holds until $Q^{(2)}$ approaches its free-space limit (dashed, light-blue curve for $a/\lambda = 0.2$). The behavior of the identical configuration is similar, but demonstrates larger $Q^{(2)}$ for small d. However, as the identical configuration

stems from few atom dark states, its $Q^{(2)}$ decreases more rapidly with growing d, rendering it preferable for nearby impurities [25].

Maximum coupling occurs between impurities in adjacent plaquettes. Fig. 4(b) displays $Q_{\max}^{(2)} \equiv Q^{(2)}(d{=}a)$. In the identical configuration, $Q_{\max}^{(2)}$ diverges as $1/a^6$ for small a, which is consistent with the $1/a^3$ dipole-dipole interaction strength that mediates the coupling enhancement and linewidth suppression of the dark state. Similarly, the orthogonal and free-space configurations exhibit a $1/a^3$ scaling, which is consistent with coupling enhancement in a system of relatively static linewidth ($\Gamma_{\text{Eff}} \approx \gamma_{\text{L}}$ for $\omega > \omega_{\text{BE}}$, see Fig. 2(b)). The size of an impurity atom network would be limited by the maximum number of lattice spacings d/a at which a desired $Q^{(2)}$ could be achieved. Fig. 4(c) shows approximately logarithmic scaling in λ/a for $Q^{(2)} > 1$.

Overall, lattice-mediated coupling improves $Q^{(2)}$ by several orders of magnitude and extends nonlinear impurity-impurity coupling to tens of lattice sites. While both configurations achieve these effects, we reemphasize that the identical and orthogonal configurations yield larger $Q^{(2)}$ for small and large d, respectively.

In conclusion, we have demonstrated that 2D atom arrays can effectively mediate between single photons and impurity atoms and have elucidated the role of polarization in these interactions. We find that 2D arrays feature superior performance to that of their 1D counterparts, as their rich, planar mode structure not only leads to the higher fidelity photon transfer required for quantum information processing, but also deterministically guides photons within the 2D plane [38], creating quantum network geometries that are infeasible in one dimension. As the optimal detuning for these coherent interactions is above the lattice band edge, the excitation can be localized near the impurity. This allows for nonlinear impurity-impurity interactions that are substantially stronger and further-reaching than those in free space, resulting in highly coherent two-atom interactions of large two-impurity quality factors $Q^{(2)}$. Such predictions could be experimentally detected by absorption measurement of individual impurity atoms or by probing time-resolved coherent dynamics of impurity atom pairs [34, 55, 56]. These results provide a framework for a multilevel treatment [57], which could extend to both array and impurity atoms and devise coherent switching, quantum gates, and guided mode excitation [27]. As the system's strong coherence and controllable dissipation display parity-time symmetry breaking [52], they apply to studies of exceptional points [58]. Finally, we note that similar effects can be explored in solid state systems, such as transition metal dichalcogenides [59], where excitons could mediate interactions between localized impurities.

We thank Arno Rauschenbeutel for insightful conversations about array-mediated strong interactions with

* taylorpatti@g.harvard.edu

[1] J. H. Kimble, Nature **453**, 1023 (2008).

[2] D. E. Chang, V. Vuletić, and M. D. Lukin, Nature Photon **8**, 685 (2014).

[3] O. Benson, Physics **10**, 42 (2017).

[4] L. Pezzè, A. Smerzi, M. K. Oberthaler, R. Schmied, and P. Treutlein, Rev. Mod. Phys. **90**, 035005 (2018).

[5] J. Ma, X. Wang, C. P. Sun, and F. Nori, Phys. Rep. **509**, 89 (2011).

[6] K. Hammerer, A. S. Sørensen, and E. S. Polzik, Rev. Mod. Phys. **82**, 1041 (2010).

[7] L. Novotny and B. Hecht. *Principles of Nano-Optics*, Cambridge University Press, Cambridge, England, (2006).

[8] E. Vetsch, D. Reitz, G. Sagué, R. Schmidt, S. T. Dawkins, and A. Rauschenbeutel, Phys. Rev. Lett. **104**, 203603 (2010).

[9] J. D. Thompson, T. G. Tiecke, N. P. de Leon, J. Feist, A. K. Akimov, M. Gullans, A. S. Zibrov, V. Vuletić, and M. D. Lukin, Science **340**, 1202 (2013).

[10] B. Gouraud, D. Maxein, A. Nicolas, O. Morin, and J. Laurat, Phys. Rev. Lett. **114**, 180503 (2015).

[11] A. Goban, K. S. Choi, D. J. Alton, D. Ding, C. Lacroûte, M. Pototschnig, T. Thiele, N. P. Stern, and H. J. Kimble, Phys. Rev. Lett. **109**, 033603 (2012).

[12] A. Reiserer and G. Rempe, Rev. Mod. Phys. **87**, 1379 (2015).

[13] A. González-Tudela, C.-L. Hung, D. E. Chang, J. I. Cirac, and H. J. Kimble, Nature Photon **9**, 320 (2015).

[14] J. S. Douglas, H. Habibian, C.-L. Hung, A. V. Gorshkov, H. J. Kimble, P. R. Hemmer, and D. E. Chang, Nature Photon **9**, 326 (2015).

[15] E. Shahmoon and G. Kurizki, Phys. Rev. A **87**, 033831 (2013).

[16] G. Calajó, F. Ciccarello, D. Chang, and P. Rabl, Phys. Rev. A **93**, 033833 (2016).

[17] J. D. Hood, A. Goban, A. Asenjo-Garcia, M. Lu, S.-P. Yu, D. E. Chang, and H. J. Kimble, PNAS **113**, 10507 (2016).

[18] L. Liu and A. A. Houck, Nature Phys **13**, 48 (2017).

[19] N. M. Sundaresan, R. Lundgren, G. Zhu, A. V. Gorshkov, and A. A. Houck, Phys. Rev. X **9**, 011021 (2019).

[20] A. Goban, C.-L. Hung, S.-P. Yu, J. D. Hood, J. A. Muniz, J. H. Lee, M. J. Martin, A. C. McClung, K. S. Choi, D. E. Chang, O. Painter, and H. J. Kimble, Nat Commun **5**, 3808 (2014).

[21] T. G. Tiecke, J. D. Thompson, N. P. de Leon, L. R. Liu, V. Vuletić, and M. D. Lukin, Nature **508**, 241 (2014).

[22] M. K. Bhaskar, R. Riedinger, B. Machielse, D. S. Levonian, C. T. Nguyen, E. N. Knall, H. Park, D. Englund, M. Lončar, D. D. Sukachev, and M. D. Lukin, Nature **580**, 60 (2020).

[23] P. Lambropoulos and D. Petrosyan. *Fundamentals of Quantum Optics and Quantum Information*, Springer, Berlin, Germany, (2007).

[24] M. Anderlini, J. Sebby-Strabley, J. Kruse, and J. V. Porto, J. Phys. B **39**, S199 (2006).

[25] See Supplemental Material at [URL will be inserted by publisher].

[26] D. E. Chang, J. S. Douglas, A. González-Tudela, C.-L. Hung, and H. J. Kimble, Rev. Mod. Phys. **90**, 031002 (2018).

[27] A. Asenjo-Garcia, M. Moreno-Cardoner, A. Albrecht, H. J. Kimble, and D. E. Chang, Phys. Rev. X **7**, 031024 (2017).

[28] Y.-X. Zhang and K. Mølmer, Phys. Rev. Lett. **122**, 203605 (2019).

[29] S. J. Masson and A. Asenjo-Garcia, Phys. Rev. Research **2**, 043213 (2020).

[30] M. Mirhosseini, E. Kim, X. Zhang, A. Sipahigil, P. B. Dieterle, A. J. Keller, A. Asenjo-Garcia, D. E. Chang, and O. Painter, Nature **569**, 692 (2019).

[31] A. Albrecht, L. Henriet, A. Asenjo-Garcia, P. B. Dieterle, O. Painter, and D. E. Chang, New J. Phys. **21**, 025003 (2019).

[32] P. Facchi, D. Lonigro, S. Pascazio, F. V. Pepe, and D. Pomarico, Phys. Rev. A **100**, 023834 (2019).

[33] E. Shahmoon, D. S. Wild, M. D. Lukin, and S. F. Yelin, Phys. Rev. Lett. **118**, 113601 (2017).

[34] J. Rui, D. Wei, A. Rubio-Abadal, S. Hollerith, J. Zeiher, D. M. Stamper-Kurn, C. Gross, and I. Bloch, Nature **583** 369374(2020).

[35] R. J. Bettles, S. A. Gardiner, and C. S. Adams, Phys. Rev. Lett. **116**, 103602 (2016).

[36] A. Grankin, P. O. Guimond, D. V. Vasilyev, B. Vermersch, and P. Zoller, Phys. Rev. A **98**, 043825 (2018).

[37] H. Zoubi and H. Ritsch, Eur. Phys. J. D **66**, 292 (2012).

[38] J. Perczel, J. Borregaard, D. E. Chang, H. Pichler, S. F. Yelin, P. Zoller, and M. D. Lukin, Phys. Rev. Lett. **119**, 023603 (2017).

[39] R. J. Bettles, S. A. Gardiner, and C. S. Adams, Phys. Rev. A **94**, 043844 (2016).

[40] E. Shahmoon, M. D. Lukin, and S. F. Yelin, Phys. Rev. A **101**, 063833(2020).

[41] I Bloch, Nature Phys **1**, 23 (2005).

[42] H. Labuhn, D. Barredo, S. Ravets, S. de de Léséleuc, T. Macrì, T. Lahaye, and A. Browaeys, Nature **534**, 667 (2016).

[43] T. Gruner, and D. G. Welsch, Phys. Rev. A. **53**, 1818 (1996).

[44] H. T. Dung, L. Knöll, and D. G. Welsch, Phys. Rev. A **66**, 063810 (2002).

[45] S. Y. Buhmann and D. G. Welsch, Prog. Quantum Electron. **31**, 51 (2007).

[46] S. Y. Buhmann, *Dispersion Forces I*, Springer-Verlag, Berlin, (2012).

[47] D. E. Chang, L. Jiang, A. V. Gorshkov, and H. J. Kimble, New J. Phys. **14**, 063003 (2012).

[48] M. Fleischhauer, A. Imamoglu, and J. P. Marangos, Rev. Mod. Phys. **77**, 633 (2005).

[49] S. Stellmer and F. Schreck, Phys. Rev. A **90**, 022512 (2014).

[50] A. G. Kofman, G. Kurizki, and B. Sherman, J. Mod. Opt. **41**, 353 (1994).

[51] R. H. Lehmberg, Phys. Rev. A **2**, 883 (1970).

[52] J. Li, A. K. Harter, J. Liu,L. de Melo, Y. N. Joglekar, and L. Luo, Nat Commun **10**, 855 (2019).

[53] N. Schuch and J. Siewert, Phys. Rev. A **67**, 032301 (2003).

[54] R.C. Bialczak, M. Ansmann, M. Hofheinz,E. Lucero, M. Neeley, A.D. O'Connell, D. Sank, H. Wang, J. Wenner, M. Steffen, A.N. Cleland, and J.M. Martinis, Nature Phys **6**, 409-413 (2010).

[55] W. S. Bakr, A. Peng, M. E. Tai, R. Ma, J. Simon, J. I. Gillen, S. Fölling, L. Pollet, and M. Greiner, Science **329**, 547 (2010).

[56] J. F. Sherson, C. Weitenberg, M. Endres, M. Cheneau, I. Bloch, and S. Kuhr, Nature **467**, 68 (2010).

[57] A. Asenjo-Garcia, H. J. Kimble, and D. E. Chang, PNAS **51**, 25503 (2019).

[58] R. El-Ganainy, K. G. Makris, M. Khajavikhan, Z. H. Musslimani, S. Rotter, and D. N. Christodoulides, Nature Physics **14**, 11 (2018).

[59] W. Choi, N. Choudhary, G. H. Han, J. Park, D. Akinwande, and Y. H. Lee, Materials Today **20**, 116 (2017).